Ordered sodium zeolite-templated carbon with high first discharge capacity for sodium battery application

Shuang Tan, Chunxu Wang, Yann Foucaud, Michael Badawi, Hailing Guo, Kun Sun, Ge Yang, Svetlana Mintova

Ordered sodium zeolite-templated carbon with high first discharge capacity for sodium battery application

Shuang Tan[a], Chunxu Wang[a], Yann Foucaud[b], Michael Badawi[c], Hailing Guo*[a], Kun Sun[a], Ge Yang[a], and Svetlana Mintova*[a, d]

[a] Shuang Tan, Chunxu Wang, Dr. H. Guo, Kun Sun, Ge Yang, Dr. S. Mintova
State Key Laboratory of Heavy Oil Processing Key Laboratory of Catalysis, China National Petroleum Corp. (CNPC) China University of Petroleum (East China) Qingdao 266555 (P.R. China) E-mail: guohl@upc.edu.cn, mintova@ensicaen.fr.
[b] Yann Foucaud
ICSM, Univ Montpellier, CEA, CNRS, ENSCM, Marcoule, France
[c] Michael Badawi
Laboratoire de Physique et Chimie Théoriques UMR CNRS 7019, Université de Lorraine, Nancy, France
[d] Dr. S. Mintova
Normandie Université, ENSICAEN, UNICAEN, CNRS, Laboratoire Catalyse et Spectrochimie (LCS), 14000 Caen, France

Abstract

A zeolite-templated carbon (ZTC) material was synthesized using a vapor phase impregnation method. This ZTC exhibited an outstandingly high specific surface area of 3,100 $m^2 \cdot g^{-1}$ along with a considerable total pore volume of 1.74 $cm^3 \cdot g^{-1}$. The properties of this ZTC were optimized by controlling the deposition process of the furfuryl alcohol, used as the carbon precursor, on the sodium-bearing zeolite Y template (FAU-type framework structure). The ZTC was then used as a negative electrode in a sodium battery setup. A high first discharge capacity of 1,714 $mAh \cdot g^{-1}$ for the ZTC was obtained, of which 16% was reversible. In addition, atomistic simulations confirmed that a theoretical capacity of 552 $mAh \cdot g^{-1}$ for the ZTC containing six sodium ions per supercage was reasonably achieved. The new vapor phase impregnation method presented here and applied for the synthesis of ZTC using sodium-bearing zeolites is highly reproducible and scalable, paving the way for the development of future applications.

Keywords

Zeolite, Carbon, Template, Vapor Phase Impregnation, Density Functional Theory.

1. Introduction

Over the past decade, Li-ion batteries (LiBs) have been increasingly used worldwide for energy storage in electronic devices. Their application ranges from

small portable equipment to electric vehicles [1-3] due to their significant lifetime and power density [4-6]. With the continued development of the LiB industry, there is significant concern that the limited terrestrial reserves of lithium will represent a major barrier for the future of LiBs. To solve this problem, the replacement of lithium with sodium has received a significant amount of interest worldwide, considering the similar storage mechanisms between LiBs and sodium ion batteries (SiBs), as well as the greater terrestrial abundance of sodium [7, 8]. However, sodium ions possess a larger radius compared to lithium ions (102 pm vs. 72 pm) meaning that the traditional graphitic carbon anode used for lithium batteries cannot be used efficiently for SiBs. This is due to the higher energy barrier of sodium intercalation into the graphite layer spacing (only 0.335 nm) [9-11]. Hence, in order to make SiBs a feasible option, it is essential to design and prepare anode materials that can store large amounts of sodium ions.

Although the traditional graphitic carbon anodes do not provide sufficient sodium ion storage, carbon materials still have great potential for SiB anodes because of their low cost, high stability, and high electrical conductivity [12-14]. Recently many studies have been devoted to the preparation of graphene nanosheets to adsorb and store sodium ions due to their significant number of edge sites and interlayer stacked mesoporous [15, 16]. Furthermore, authors have also investigated the storage of sodium ions using the domain-limited space of three-dimensional carbon structures such as carbon spheres [11] and 3D porous carbon frameworks [13]. A recent study about the storage mechanisms of sodium ions in hard carbon materials obtained by the pyrolysis of hydrothermally-treated sucrose assumed that the formation of pseudo-metallic sodium in the material nanopores is the key to the reversible capacity of hard carbon materials [17].

Zeolite-templated carbon (ZTC), which corresponds to an ordered microporous carbon material possessing the properties of zeolites such as their structural diversity and adjustable pores, has drawn worldwide attention since it was firstly reported [18]. The abundant interconnected micropores of ZTC could provide sites to form pseudo-metallic sodium and, therefore, could provide a high reversible capacity for anodes of SiBs. Despite that the ZTC has the potential of providing high sodium ion storage capacity, the application as a battery electrode material is under consideration. However, the main problem in the preparation of ZTC is the complex preparation process involving the deposition of the carbon precursor, carbonization, and the removal of the zeolite template [19-23]. The controllable deposition of the carbon precursor is the critical stage of the preparation process of the ZTC. This involves homogeneously covering the inner and outer surfaces of the zeolite with the carbon precursors, representing the most challenging step.

The most common methods for deposition of carbon precursors on zeolites are liquid impregnation [18, 24-28][18, 24-28], chemical vapor deposition (CVD) [22, 29-33], and a combination of liquid phase impregnation and CVD (a two-step method) [34-37]. Compared to CVD, liquid phase impregnation was reported as a much simpler process and with a higher scale-up potential. However, the ZTC materials prepared by the liquid phase impregnation method generally present a relatively low

specific surface area (590-1440 $m^2 \cdot g^{-1}$), low total pore volume (0.43-1.17 $cm^3 \cdot g^{-1}$), low microporosity (60-79%) and a certain mesoporosity [38-40]. These characteristics are due to the incomplete filling of the zeolite pores by the highly viscous carbon precursors, and therefore traditionally requiring a high vacuum to fill the zeolite pores entirely. The additional processing steps are also of great importance and affect the properties of the ZTC: (1) the washing stage, to remove the excess carbon precursor, influences the development of the outer carbon layer of the ZTC [20], (2) the calcination process significantly affects the degree of graphitization and the structural integrity of the ZTC [23], and (3) the de-templating phase can also alter the surface charge of the ZTC [41]. Therefore, a simple preparation method with a high reproducibility and a high scale-up potential is highly desirable for the preparation of ZTC materials which would enable further application development.

In this work, we present a new vapor phase impregnation method to prepare highly-ordered ZTC material using a sodium-bearing zeolite as the template (Y zeolite with FAU type framework structure) and furfuryl alcohol (FA) as the carbon precursor. The simple ZTC preparation method was then scaled up, the ZTC samples with highly-ordered microporous structure were then assembled on a negative electrode of a sodium battery, and their performance was studied using experimental and theoretical techniques.

2. Materials and methods

2.1 Preparation of the ZTC samples

We used a faujasite-type (FAU) zeolite (Si/Al=7.55, Na content of 9.27 wt.%) supplied by Nankai university catalyst Co., Ltd, Furfuryl alcohol (AR, 98%) acquired from Macklin, mesitylene (CP, 97%) supplied by Aladdin, and hydrofluoric acid (40 wt.%) and hydrochloric acid (38 wt.%) both provided by Sinopharm chemical reagent Co., Ltd.

The ZTC synthesis protocol is presented in Fig. 1. The FAU-zeolite powder sample was first activated at 300 °C to remove the physisorbed water. Then, a representative sample of 5 g of the activated FAU-zeolite powder was used for the preparation of the ZTC by placing it into a reactor equipped with a sand-core that allows the vapor to pass through; this reactor was connected to a flask containing the FA, which was the carbon precursor. The whole system was kept under vacuum during all the vapor phase impregnation process. Then, the FA was heated at 100 °C and the generated FA vapor passed through the sand-core and adsorbed in the channels of the zeolite. Once the zeolite was saturated with FA, nitrogen was introduced to restore the atmospheric pressure. The sample was maintained for 24 hours under these conditions before removing the FA that was adsorbed on the external surface by washing with mesitylene. The excess of mesitylene was removed by heating at 80 °C for 24 h and the FA-loaded zeolite was further heated at 150 °C for 8 h under a nitrogen atmosphere to pre-polymerize the FA. The pre-polymerized samples were then calcined at 800, 900, and 1000 °C for 4 h and labeled as FAU-P-X,

where X referred to the calcination temperature (X = 800, 900, 1000); a heating rate of 5 °C·min^{-1} under a nitrogen atmosphere was applied for this stage. Finally, all samples were washed with a solution of 0.4 mol·L^{-1} HF + 0.2 mol·L^{-1} HCl and with distilled water, before being dried at 100 °C overnight. Samples after de-templating were labeled as FAU-ZTC-X, where X referred to the calcination temperature (X = 800, 900, 1000). The scale-up of this procedure was carried out using 20 g of FAU-zeolite template; the sample was labeled FAU-ZTC-900-S.

2.2 Characterization

The morphology and crystal size of the samples were characterized using a JEOL SEM-7900F scanning electron microscope (SEM) with an acceleration voltage of 5 kV. X-ray powder diffraction (XRD) patterns were collected using a Bruker D8 Advance. The N_2 adsorption-desorption experiments were performed at 77 K using a Quantachrome Autosorb iQ3 gas-sorption analyzer. The BET specific surface area was calculated from the range in P/P_0 = 0.02-0.15 while the total pore volume was determined at P/P_0 = 0.97 and the micropore volume was calculated from *v-t* plot at P/P_0 = 0.4-0.6. The pore size distribution was determined using the Quenched solid density functional theory (QSDFT) method. Thermogravimetry measurements were performed by a NETZSCH (STA 449 F5) at 5 ºC·min^{-1} heating rate in the temperature range 20-900 °C under an air atmosphere.

2.3 Electrochemical measurements

The electrochemical performance of the ZTC samples was evaluated using half-cells assembled in a glove box. The sample powder was mixed with super P and poly vinylidene fluoride in a weight ratio of 8:1:1 in N-methyl-2-pyrrolidinone to form a homogeneous slurry, which was then deposited into a layer with a thickness of 30 μm on a Cu foil and dried in a vacuum oven at 80 °C for 12 h. Sodium metal foils were used as counter and reference electrodes. A solution of 1 mol·L^{-1} $NaClO_4$ in ethylene carbonate/diethyl carbonate (1/1; v/v) with 5 wt.% fluoroethylene carbonate was used as the electrolyte and Celgard 2400 was used as the separator. The active materials mass loading on each round Cu foil was about 0.7 mg·cm^{-2}. Cyclic voltammetric measurements with a scan rate of 0.1 mV·s^{-1} were performed on a CHI760D electrochemical workstation. Galvanostatic charge/discharge measurements were performed using a multichannel battery testing system (LAND CT2001A) in a voltage range of 0.01–3 V for anodes versus Na/Na^+ at different constant current densities.

2.4 DFT calculations

All the static DFT relaxations and *ab initio* molecular dynamics (AIMD) simulations were carried out using the Vienna Ab Initio Simulation program [42, 43], with the semi-local Perdew-Burke-Ernzerhof exchange-correlation functional [44]. The electron-ion interactions were described by the projector-augmented wave method with a plane wave cutoff kinetic energy of 350 eV for the AIMD simulations

and 600 eV for the static DFT calculations. The Kohn-Sham equations were solved self-consistently until the energy difference between cycles was lower than 10^{-7} eV for the static calculation and lower than 10^{-4} eV for the AIMD simulations. All the calculations were performed using the Γ-point only considering the large size of the cell. The D2 correction of Grimme [45, 46] was used to take van der Waals forces into account. The charge of the Na^+ ion(s) was systematically compensated by adding a homogeneous negative background charge [47]. The modeling procedure [42] was as follows: (i) a ZTC model composed of 629 carbon atoms, organized in 5-, 6-, 7-, 8-, and 9-membered rings, was generated and fully relaxed [48, 49] (in terms of atom positions, cell size, and cell shape). After the full optimization, the cell parameters of the model were a = 24.87 Å, b = 24.36 Å, c = 24.94 Å, α = 91.09°, β = 90.18°, and γ = 88.90°; (ii) a given number of Na^+ ions were placed in the ZTC model and an AIMD simulation was carried out during 10 ps to determine the most visited configuration for their adsorption; and (iii) on the most visited configuration, a static DFT calculation was performed to determine the adsorption energy of the considered Na^+ ion in the ZTC by comparing the energy of the system where the Na^+ ion is adsorbed on the ZTC to that where the Na^+ ion is in the middle of the cage. The successive adsorption energy of Na^+ ions was determined.

3. Result and discussions

3.1 Characterization of the ZTC

The XRD patterns of the ZTC samples in comparison to the parent FAU-zeolite template are presented in Fig. 2A. The ZTC samples display a Bragg peak at 6.3° 2θ that corresponds to the FAU-type zeolite framework structure [26]. The position and intensity of the peak at 6.3° 2θ suggest that the FAU structure of the ZTC is preserved, which is induced by the complete filling of the zeolite pores using the vapor phase impregnation method. However, the conventional liquid impregnation method usually results in the incomplete filling of the pores and the pyrolysis of the small molecules at high temperature causes the disorder of the carbon framework, preventing the formation of long-range ordered microporous ZTC [18, 20]. No diffraction peak at 25° 2θ with *hkl* of (002) expected for the turbostratic carbon is observed for all the analyzed ZTC samples. This indicates that the FA adsorbed on the external surface of the zeolite crystals was completely removed, avoiding the formation of external carbon layers. When the CVD deposition method is used a strict control of the operating conditions is required to avoid the formation of external carbon layers [22, 23, 50]. Using the TG analysis, the carbon content in the zeolite was estimated to be 0.28 g/g, which is much higher than the carbon loaded by conventional impregnation (0.12 g/g zeolite) [51], slightly higher than using the CVD method (0.24 g/g zeolite),[22, 32] and lower than the two-step approach (0.30 g/g zeolite) [22, 52].

The parent FAU zeolite and the ZTC samples are shown in Fig. 2B and Fig. S1. All the ZTC samples contain intergrown crystals that are identical to that observed for the parent FAU-zeolite. The typical octahedral morphology of the individual crystals

with a size of 1 μm can be seen both in the parent FAU and in the ZTC samples, which confirms the templating role of the zeolite crystals and the complete replication. The FAU-ZTC-800 sample, in comparison to the FAU-ZTC-900 sample, has a flatter facet and sharper edges. Higher mass loss originating from the carbon precursor under treatment at higher temperature might be responsible for this phenomenon as reported previously [20]. This effect was further confirmed for the FAU-ZTC-1000 sample where the mass loss also caused the carbon skeleton folding [53] resulting in crystals with a starfish-like appearance.

The Raman spectra of the ZTC samples contain two peaks at 1350 cm^{-1} and 1600 cm^{-1} which are attributed to the D and G bands of graphite respectively (Fig. 2C). The D band (I_D) is related to the A_{1g} ring-breathing mode, which is an indicator of the defects or lattice disorders in the graphene structure, while the G band (I_G) is ascribed to the E_{2g} vibration mode of the relative motion between sp^2 carbon atoms [37]. The I_D/I_G ratio of FAU-ZTC-800, FAU-ZTC-900, and FAU-ZTC-1000 samples are 0.655, 0.785, and 0.859, respectively, which indicates that increasing the carbonization temperature from 800 to 1000 °C results in a decrease of the ordering of the ZTC samples. Based on the XRD results, the optimal pyrolysis temperature range is selected for maintaining the spatial structure of the ZTC. The high temperature (1000 °C) is unfavorable for maintaining the ZTC order which can be explained by the different thermal expansion of the carbon and the zeolite template [19, 23, 54].

The porosity of the ZTC samples is characterized by N_2 physisorption measurements (Fig. 3A). All the isotherms are type I according to IUPAC classification indicating the presence of micropores in the samples. The increase of the carbonization temperature induces a significant increase of the total pore volume except for the FAU-ZTC-1000 sample (Table 1). This result is in agreement with the XRD (Fig. 2A), which highlighted the low crystalline order of the FAU-ZTC-1000 sample. The ZTC samples exhibit very high BET specific surface area in the range of 1400-3100 $m^2 \cdot g^{-1}$, which is much higher than the specific surface area of the pure FAU zeolite template (869 $m^2 \cdot g^{-1}$). The pore size distribution of the ZTC samples is presented in Fig. 3B. The narrow pore size distribution can be ascribed to the periodically-ordered ZTC structure. Among all the considered samples, the FAU-ZTC-900 sample presents the highest porosity, with a surface area of 3102 $m^2 \cdot g^{-1}$ and a total pore volume of 1.75 $cm^3 \cdot g^{-1}$. The porosity of the FAU-ZTC-900 sample is much higher than that of the activated carbon and the parent FAU zeolite, and close to the ZTC material prepared by the “two-step” method [37]. The carbon and moisture contents in the initial precursor mixtures (FAU-P-X, where X = 800, 900, or 1000 °C) and in the ZTC samples (FAU-ZTC-X, where X = 800, 900, and 1000 °C) are summarized in Table 2.

The vapor phase impregnation method used for the preparation of ZTC has then been scaled up. In contrast to the usual weight of zeolite template applied in the experiments described above, 20 g of zeolite powder was used. The XRD pattern and SEM photograph of the scaled-up FAU-ZTC-900-S sample are presented in Fig. S2.

The FAU-ZTC-900-S sample is identical to the FAU-ZTC-900, which confirms the reproducibility of the synthesis procedure.

3.2 Storage capacity

The ZTC sample with high surface area and uniform micropores was considered for the application in the field of ion storage. The sodium storage performance of sample FAU-ZTC-900 was evaluated after assembly into 2032 Na/ZTC half-cells. The initial five cyclic voltammograms of the electrode composed of the FAU-ZTC-900 sample at $0.1 mV \cdot s^{-1}$ within a potential range of 0.01 V – 3.0 V are presented in Fig. 4A. Three irreversible peaks at 0.01 V, 0.86 V, and 1.22 V appear during the first cycle. The cathodic peak at 0.01 V is attributed to the insertion or nanopore filling of sodium ions into the carbon materials [13]. However, the XRD results demonstrate that no stacked graphite structure is present in the ZTC and, therefore, the peak at 0.01 V probably results from the filling of the supercage of the FAU-ZTC structure by sodium ions. Meanwhile, the peaks at 0.86 V and 1.22 V disappear in the second cycle which is probably due to an irreversible reaction between Na^+ and the FAU-ZTC-900. This leads to the decomposition of propylene carbonate electrolyte and the formation of solid electrolyte interface (SEI) layers[10, 11, 13]. This causes the massive irreversible capacity as shown in the galvanostatic charge-discharge curve (Fig. 4B). The first discharge and charge capacities for sample FAU-ZTC-900 at a current density of 100 $mA \cdot g^{-1}$ are 1714.0 and 288.1 $mAh \cdot g^{-1}$, respectively. The specific capacity loss also brings a low initial Coulombic efficiency. The absence of charge peaks in the cyclic voltammograms indicates that sodium ions are seldom extracted or with a negligibly low rate. The sodium ions adsorbed on the surface provide the main high voltage discharge capacity while the onces in the pores contribute to the main low voltage discharge capacity (0.01-0.3 V) in the first discharge. However, no plateau in the low-pressure region in the subsequent charging curves is observed. This suggests that the storage behavior of sodium ions in the ZTC is no longer dominated by pore filling, but is more inclined to surface adsorption. This finding is in an agreement with the CV results. The subsequent cycle analysis of sample FAU-ZTC-900 shows that the specific capacity is fully preserved (100%) after 10 cycles (Fig. 4C). After 60 cycles, the reversible capacity stabilizes at about 170 $mAh \cdot g^{-1}$, this value is better than most conventional carbon material SIB cathodes (Table S1). The irreversible capacity of ZTC in SiBs (84%) is higher compared to the LiBs (41%); a large amount of Li^+ remained inside the ZTC resulting in a large amount of irreversible capacity[55]. In the present work the $NaClO_4$ electrolyte, possessing a small molecular diameter, may lead to a thicker SEI layer that may consume a high amount of Na^+. Moreover, the larger radius of Na ions is another factor responsible for the higher irreversible capacity of the ZTCs in SiBs compared to LiBs. The rate performance characteristics of the FAU-ZTC-900 sample at different current densities were investigated. The FAU-ZTC-900 showed excellent reversible capacity of 262, 205, 164, 117, 101, 87 and 68 mAh·g-1 at 50, 100, 200, 500, 1000, 2000 and 5000 mAg-1, respectively (Fig. 4D). The charging capacity of FAU-ZTC-900 can be recovered to 207 mAh/g at 0.05 A/g after charging and

discharging at 5A/g. The results demonstrated the high structural stability of the FAU-ZTC-900 sample.

3.3 DFT calculations

According to Ryong Ryoo's calculations [55], an initial capacity of 1714 $mAh \cdot g^{-1}$ implies that 19.6 sodium ions are accommodated in the FAU supercage. Due to the large diameter of sodium ions and the limited volume of the supercages of ZTC, this loading is barely achievable. Apparently, the sodium ions forming the SEI layer contribute to the irreversible capacity. In contrast, the second discharge capacity of 288 $mAh \cdot g^{-1}$ and the stable reversible capacity of 170 $mAh \cdot g^{-1}$ determined by our experiments imply reversible adsorption and desorption of 3.1 and 1.9 sodium ions respectively in the ZTC supercage. To gain understanding of the adsorption and desorption of sodium ions from the ZTC supercages AIMD simulations followed by DFT calculations were performed. When the ZTC pore filling degree is increased the sodium cations do not form spontaneously metallic or pseudo-metallic forms. Indeed, when the ions are initially placed in a metallic configuration in the supercage, *i.e.*, with $d_{Na\text{-}Na}$ = 3.72 Å, they move away during the static DFT relaxation. This result is observed for 2, 3, 4, and 7 Na^+ ions, which indicates that no metallic sodium cluster is thermodynamically stable in the ZTC supercage. A single sodium ion adsorbs with ΔE_{ads} = -196.9 $kJ \cdot mol^{-1}$ including ΔE_{disp} = -40.8 $kJ \cdot mol^{-1}$; the high adsorption energy could explain the irreversibility of the adsorption of sodium ions in the ZTC supercages. The adsorption of each sodium ion in the ZTC supercage occurs with 2 Na-C bonds established with a distance ($d_{Na\text{-}C}$) between 2.5 Å and 2.6 Å (Fig. 5). When the filling degree of the supercage with sodium ions increases, the adsorption energy slightly decreases to -150 and -160 $kJ \cdot mol^{-1}$. Then, the adsorption energy stays constant with increasing the number of sodium ions until seven sodium ions before gradually decreasing to attain 0 $kJ \cdot mol^{-1}$ for 48 sodium ions. The surface of the ZTC supercage is progressively covered by Na^+ ions when the filling degree increases and the average Na-Na distance decreases. For 48 Na^+, some Na-Na bonds are observed and clusters involving several sodium atoms are formed for 96 and 144 sodium ions. This is consistent with the decrease of the available surface for adsorption, although this clustering is clearly endothermic considering the significant decrease of the absolute value of the adsorption energy with the coverage. The adsorption model with 48 sodium ions, *i.e.*, with an average of 6 sodium ions are accommodated in each supercage, would represent a high reversible capacity of 553 $mAh \cdot g^{-1}$ if all of them could be desorbed. This value has neither been reported so far [56] nor attained by experimental techniques, which indicates that some of these sodium ions are not able to be completely desorbed because of their high adsorption energy, which constitutes an irreversible capacity. By assuming that only 3.1 and 1.9 sodium ions can be freely adsorbed and desorbed respectively, based on our experimental results, we can assess that only the sodium ions adsorbed with an adsorption energy lower than -100 $kJ \cdot mol^{-1}$ in absolute value can be desorbed. Hence, a reversible activation of the remaining inert sodium should be considered in the future.

4. Conclusion

A vapor phase impregnation method was developed for the preparation of a long-range microporous carbon with a high specific surface area (3100 $m^2 \cdot g^{-1}$) and a high pore volume (1.74 $cm^3 \cdot g^{-1}$) using a FAU-type zeolite as a template. Compared with the traditional liquid impregnation and CVD methods, the vapor phase impregnation method presented here displays the following advantages: (i) an accurate control of the internal and external surfaces during the FA carbon precursor deposition process can be achieved; (ii) a long-range ordered carbon structure with high microporosity can be obtained; and (iii) a scalable and reproducible methodology for the preparation of ZTC is developed.

The generated ZTC exhibits an outstandingly high first discharge capacity (1714 $mAh \cdot g^{-1}$) and a high reversible capacity for a carbon material. Cyclic voltammograms show that nanopore filling is the main mechanism of storing sodium ions in ZTC. The rich microporous structure and the high specific surface area of ZTC provides plenty of sites for sodium ion storage, but also results in a large number of SEI layers. This, coupled with the complex and narrow pore structure which makes the complete sodium ion desorption difficult, induces a very low first-cycle Coulombic efficiency for the generated ZTC. Furthermore, DFT calculations indicate that the ZTC material has a theoretical reversible capacity of at least 553 $mAh \cdot g^{-1}$, although the first sodium ions are adsorbed with very high adsorption energies in absolute values. Efficient utilization of the sodium ions irreversibly adsorbed in the supercages is the key to further improvement in the reversible capacity of ZTC.

ACKNOWLEDGMENT

The authors gratefully acknowledged funding from the National Natural Science Foundation of China [Grant No. U1862118, No. 21975285, No. 21991091, No. 22175200], the Fundamental Research Funds for the Central Universities [No. 21CX06024A], the State Key Laboratory of Advanced Technology for Materials Synthesis and Processing (Wuhan University of Technology) [No. 2018-KF-13], and appreciate the support from the Foundation Franco-Chinoise pour la Science et Applications (FFCSA) and the Sino-French LIA “Zeolite”.

REFERENCES

[1] B. Wang, T. Xu, S. Huang, D. Kong, X. Li, Y. Wang, Recent advances in carbon-shell-based nanostructures for advanced Li/Na metal batteries, J. Mater. Chem. A, 9 (2021) 6070-6088.

[2] F. Ding, W. Xu, G.L. Graff, J. Zhang, M.L. Sushko, X. Chen, Y. Shao, M.H. Engelhard, Z. Nie, J. Xiao, X. Liu, P.V. Sushko, J. Liu, J.-G. Zhang, Dendrite-Free Lithium Deposition via Self-Healing Electrostatic Shield Mechanism, J. Am. Chem. Soc., 135 (2013) 4450-4456.

[3] G.M. Zhou, F. Li, H.M. Cheng, Progress in flexible lithium batteries and future prospects, Energ. Environ. Sci., 7 (2014) 1307-1338.
[4] M. Armand, J.M. Tarascon, Building better batteries, Nature, 451 (2008) 652-657.
[5] H. Jiang, D. Ren, H. Wang, Y. Hu, S. Guo, H. Yuan, P. Hu, L. Zhang, C. Li, 2D Monolayer MoS2–Carbon Interoverlapped Superstructure: Engineering Ideal Atomic Interface for Lithium Ion Storage, Adv. Mater., 27 (2015) 3687-3695.
[6] H. Wang, J. Wang, D. Cao, H. Gu, B. Li, X. Lu, X. Han, A.L. Rogach, C. Niu, Honeycomb-like carbon nanoflakes as a host for SnO_2 nanoparticles allowing enhanced lithium storage performance, J. Mater. Chem. A, 5 (2017) 6817-6824.
[7] X. Li, X.-y. Wang, J. Sun, Recent progress in the carbon-based frameworks for high specific capacity anodes/cathode in lithium/sodium ion batteries, New Carbon Mater., 36 (2021) 106-116.
[8] Y. Zhong, Q. Shi, C. Zhu, Y. Zhang, M. Li, J.S. Francisco, H. Wang, Mechanistic Insights into Fast Charging and Discharging of the Sodium Metal Battery Anode: A Comparison with Lithium, J. Am. Chem. Soc., 143 (2021) 13929-13936.
[9] S. Wenzel, T. Hara, J. Janek, P. Adelhelm, Room-temperature sodium-ion batteries: Improving the rate capability of carbon anode materials by templating strategies, Energ. Environ. Sci., 4 (2011) 3342-3345.
[10] Y. Cao, L. Xiao, M.L. Sushko, W. Wang, B. Schwenzer, J. Xiao, Z. Nie, L.V. Saraf, Z. Yang, J. Liu, Sodium ion insertion in hollow carbon nanowires for battery applications, Nano Lett., 12 (2012) 3783-3787.
[11] K. Tang, L. Fu, R.J. White, L. Yu, M.-M. Titirici, M. Antonietti, J. Maier, Hollow Carbon Nanospheres with Superior Rate Capability for Sodium-Based Batteries, Adv. Energy Mater., 2 (2012) 873-877.
[12] C. Ling, F. Mizuno, Boron-doped graphene as a promising anode for Na-ion batteries, Phys. Chem. Chem. Phys., 16 (2014) 10419-10424.
[13] H. Hou, C.E. Banks, M. Jing, Y. Zhang, X. Ji, Carbon Quantum Dots and Their Derivative 3D Porous Carbon Frameworks for Sodium-Ion Batteries with Ultralong Cycle Life, Adv. Mater., 27 (2015) 7861-7866.
[14] Y. Li, Y.-S. Hu, M.-M. Titirici, L. Chen, X. Huang, Hard Carbon Microtubes Made from Renewable Cotton as High-Performance Anode Material for Sodium-Ion Batteries, Adv. Energy Mater., 6 (2016) 1600659.
[15] D.W. Su, S.X. Dou, G.X. Wang, Ultrathin MoS_2 Nanosheets as Anode Materials for Sodium-Ion Batteries with Superior Performance, Adv. Energy Mater., 5 (2015) 1401205.
[16] J.L. Xia, D. Yan, L.P. Guo, X.L. Dong, W.C. Li, A.H. Lu, Hard Carbon Nanosheets with Uniform Ultramicropores and Accessible Functional Groups Showing High Realistic Capacity and Superior Rate Performance for Sodium-Ion Storage, Adv. Mater., 32 (2020) 2000447.
[17] Y. Morikawa, S.i. Nishimura, R.i. Hashimoto, M. Ohnuma, A. Yamada, Mechanism of Sodium Storage in Hard Carbon: An X- Ray Scattering Analysis, Adv. Energy Mater., 10 (2019) 1903176.
[18] T. Kyotani, T. Nagai, S. Inoue, A. Tomita, Formation of New Type of Porous Carbon by Carbonization in Zeolite Nanochannels, Chem. Mater, 9 (1997) 609-615.

[19] T. Kyotani, Control of pore structure in carbon, Carbon, 30 (2000) 269-286.
[20] Z. Ma, T. Kyotani, A. Tomita, Synthesis methods for preparing microporous carbons with a structural regularity of zeolite Y, Carbon, 40 (2002) 2367-2374.
[21] J. Parmentier, V. Valtchev, F. Gaslain, L. Tosheva, C. Ducrot-Boisgontier, J. Möller, J. Patarin, C. Vix-Guterl, Effect of the zeolite crystal size on the structure and properties of carbon replicas made by a nanocasting process, Carbon, 47 (2009) 1066-1073.
[22] Y. Xia, Z. Yang, R. Mokaya, CVD Nanocasting Routes to Zeolite-Templated Carbons for Hydrogen Storage, Chem. Vapor Depos., 16 (2010) 322-328.
[23] R.J. Konwar, M. De, Effects of synthesis parameters on zeolite templated carbon for hydrogen storage application, Micropor. Mesopor. Mat., 175 (2013) 16-24.
[24] Z. Ma, T. Kyotani, A. Tomita, Preparation of a high surface area microporous carbon having the structural regularity of Y zeolite, Chem. Commun., (2000) 2365-2366.
[25] Z. Ma, T. Kyotani, Z. Liu, O. Terasaki, A. Tomita, Very High Surface Area Microporous Carbon with a Three-Dimensional Nano-Array Structure: Synthesis and Its Molecular Structure, Chem. Mater., 13 (2001) 4413-4415.
[26] T. Kyotani, Z. Ma, A. Tomita, Template synthesis of novel porous carbons using various types of zeolites, Carbon, 41 (2003) 1451-1459.
[27] F. Su, X.S. Zhao, L. Lv, Z. Zhou, Synthesis and characterization of microporous carbons templated by ammonium-form zeolite Y, Carbon, 42 (2004) 2821-2831.
[28] A. Garsuch, O. Klepel, Synthesis of ordered carbon replicas by using Y-zeolite as template in a batch reactor, Carbon, 43 (2005) 2330-2337.
[29] F.O. Gaslain, J. Parmentier, V.P. Valtchev, J. Patarin, First zeolite carbon replica with a well resolved X-ray diffraction pattern, Chem Commun (Camb), (2006) 991-993.
[30] Z. Yang, Y. Xia, R. Mokaya, Enhanced Hydrogen Storage Capacity of High Surface Area Zeolite-like Carbon Materials, J. Am. Chem. Soc, 129 (2007) 1673-1679.
[31] H. Itoi, H. Nishihara, T. Kogure, T. Kyotani, Three-dimensionally arrayed and mutually connected 1.2-nm nanopores for high-performance electric double layer capacitor, J. Am. Chem. Soc., 133 (2011) 1165-1167.
[32] S. Choi, H. Kim, S. Lee, Y. Wang, C. Ercan, R. Othman, M. Choi, Large-scale synthesis of high-quality zeolite-templated carbons without depositing external carbon layers, Chem. Eng. J., 280 (2015) 597-605.
[33] K. Kim, T. Lee, Y. Kwon, Y. Seo, J. Song, J.K. Park, H. Lee, J.Y. Park, H. Ihee, S.J. Cho, R. Ryoo, Lanthanum-catalysed synthesis of microporous 3D graphene-like carbons in a zeolite template, Nature, 535 (2016) 131-135.
[34] R. Berenguer, H. Nishihara, H. Itoi, T. Ishii, E. Morallón, D. Cazorla-Amorós, T. Kyotani, Electrochemical generation of oxygen-containing groups in an ordered microporous zeolite-templated carbon, Carbon, 54 (2013) 94-104.
[35] J. Zhou, W. Li, Z. Zhang, X. Wu, W. Xing, S. Zhuo, Effect of cation nature of zeolite on carbon replicas and their electrochemical capacitance, Electrochim. Acta, 89 (2013) 763-770.

[36] N.M. Musyoka, J. Ren, H.W. Langmi, D.E.C. Rogers, B.C. North, M. Mathe, D. Bessarabov, Synthesis of templated carbons starting from clay and clay-derived zeolites for hydrogen storage applications, Int. J. Energ. Res, 39 (2015) 494-503.
[37] N.P. Stadie, S. Wang, K.V. Kravchyk, M.V. Kovalenko, Zeolite-Templated Carbon as an Ordered Microporous Electrode for Aluminum Batteries, ACS Nano, 11 (2017) 1911-1919.
[38] H. Nishihara, T. Kyotani, Zeolite-templated carbons - three-dimensional microporous graphene frameworks, Chem Commun (Camb), 54 (2018) 5648-5673.
[39] J. Miao, Z. Lang, T. Xue, Y. Li, Y. Li, J. Cheng, H. Zhang, Z. Tang, Revival of Zeolite-Templated Nanocarbon Materials: Recent Advances in Energy Storage and Conversion, Adv Sci (Weinh), 7 (2020) 2001335.
[40] E.E. Taylor, K. Garman, N.P. Stadie, Atomistic Structures of Zeolite-Templated Carbon, Chem. Mater., 32 (2020) 2742-2752.
[41] H. Park, S.K. Terhorst, R.K. Bera, R. Ryoo, Template dissolution with NaOH–HCl in the synthesis of zeolite-templated carbons: Effects on oxygen functionalization and electrical energy storage characteristics, Carbon, 155 (2019) 570-579.
[42] A. Geneyton, Y. Foucaud, L.O. Filippov, N.E. Menad, A. Renard, M. Badawi, Synergistic adsorption of lanthanum ions and fatty acids for efficient rare-earth phosphate recovery: Surface analysis and ab initio molecular dynamics studies, Appl. Surf. Sci., 526 (2020) 146725.
[43] J. Hafner, Ab-initio simulations of materials using VASP: Density-functional theory and beyond, J. Comput. Chem., 29 (2008) 2044-2078.
[44] J.P. Perdew, K. Burke, M. Ernzerhof, Generalized Gradient Approximation Made Simple, Phys. Rev. Lett., 77 (1996) 3865-3868.
[45] S. Grimme, Semiempirical GGA-type density functional constructed with a long-range dispersion correction, J. Comput. Chem., 27 (2006) 1787-1799.
[46] T. Bučko, J. Hafner, S. Lebègue, J.G. Ángyán, Improved Description of the Structure of Molecular and Layered Crystals: Ab Initio DFT Calculations with van der Waals Corrections, J. Phys. Chem. Lett. A, 114 (2010) 11814-11824.
[47] Y. Foucaud, J. Lainé, L.O. Filippov, O. Barrès, W.J. Kim, I.V. Filippova, M. Pastore, S. Lebègue, M. Badawi, Adsorption mechanisms of fatty acids on fluorite unraveled by infrared spectroscopy and first-principles calculations, J. Colloid Interf. Sci., 583 (2021) 692-703.
[48] T. Roussel, A. Didion, R.J.M. Pellenq, R. Gadiou, C. Bichara, C. Vix-Guterl, Experimental and Atomistic Simulation Study of the Structural and Adsorption Properties of Faujasite Zeolite−Templated Nanostructured Carbon Materials, J. Phys. Chem. Lett. C, 111 (2007) 15863-15876.
[49] S. Builes, T. Roussel, C.M. Ghimbeu, J. Parmentier, R. Gadiou, C. Vix-Guterl, L.F. Vega, Microporous carbon adsorbents with high CO2 capacities for industrial applications, Phys. Chem. Chem. Phys., 13 (2011) 16063-16070.
[50] C. Yong Liang Guana, A. Elkamel, K. Wang, Energy gas storage in template-synthesized carbons with different porous structures, Can. J. Chem. Eng., 93 (2015) 527-531.

[51] F. Su, L. Lv, T.M. Hui, X.S. Zhao, Phenol adsorption on zeolite-templated carbons with different structural and surface properties, Carbon, 43 (2005) 1156-1164.
[52] R.J. Dubey, J. Nussli, L. Piveteau, K.V. Kravchyk, M.D. Rossell, M. Campanini, R. Erni, M.V. Kovalenko, N.P. Stadie, Zeolite-Templated Carbon as the Cathode for a High Energy Density Dual-Ion Battery, ACS Appl Mater Interfaces, 11 (2019) 17686-17696.
[53] T. Lee, S.H. Ko, S.J. Cho, R. Ryoo, Ultramicroporous Carbon Synthesis Using Lithium-Ion Effect in ZSM-5 Zeolite Template, Chem. Mater., 30 (2018) 6513-6520.
[54] H. Nishihara, K. Imai, H. Itoi, K. Nomura, K. Takai, T. Kyotani, Formation mechanism of zeolite-templated carbons, Tanso, 2017 (2017) 169-174.
[55] Y. Kwon, K. Kim, H. Park, J.W. Shin, R. Ryoo, Anomalously High Lithium Storage in Three-Dimensional Graphene-like Ordered Microporous Carbon Electrodes, J. Phys. Chem. Lett. C, 122 (2018) 4955-4962.
[56] D. Chen, W. Zhang, K. Luo, Y. Song, Y. Zhong, Y. Liu, G. Wang, B. Zhong, Z. Wu, X. Guo, Hard carbon for sodium storage: mechanism and optimization strategies toward commercialization, Energ. Environ. Sci., 14 (2021) 2244-2262.

TABLES

Table 1 Textural properties of parent FAU zeolite and ZTC samples.

Sample	S_{BET} ($m^2 \cdot g^{-1}$)[a]	V_t ($cm^3 \cdot g^{-1}$)[b]	V_{mi} ($cm^3 \cdot g^{-1}$)[c]	R_{mi} [d]
Parent FAU	869	0.39	0.32	0.95
FAU-ZTC-800	2106	1.17	0.72	0.61
FAU-ZTC-900	**3102**	**1.75**	**1.08**	**0.61**
FAU-ZTC-1000	1452	0.91	0.51	0.56

[a] BET specific surface area was calculated from the adsorption branch in P/P_0 = 0.02-0.15.

[b] Total pore volume was determined at P/P_0 = 0.97.

[c] Micropore volume was calculated from v-t plot at P/P_0 = 0.4-0.6.

[d] Ratio of micropore to total volumes.

Table 2 Carbon and moisture contents in the initial precursor mixtures (FAU-P-X, where X = 800, 900, and 1000 °C) and in the ZTC samples (FAU-ZTC-X, where X = 800, 900, and 1000 °C).

	FAU-P-800	FAU-P-900	FAU-P-1000	FAU-ZTC-800	FAU-ZTC-900	FAU-ZTC-1000
Moisture (wt.%)[a]	5.5	4.5	6.2	7.4	6.1	8.8
Carbon content (wt.%)[b]	22.5	22.0	22.8	98.0	98.4	93.0
Carbon ratio ($g \cdot (g\ of\ zeolite)^{-1}$)[c]	29.1	28.2	29.6	-	-	-

[a] determined by the weight loss of samples (20-200 °C)

[b] determined by the weight loss of samples (200-900 °C)

[c] Ratio of carbon weight to zeolite weight in a FAU-P-X sample

FIGURE CAPTIONS

Fig. 1. Schematic illustration of vapor phase impregnation process applied in this work for the preparation of the ZTC.

Fig. 2. XRD patterns (A), SEM pictures (B), and Raman spectra (C) of (a) parent FAU, (b) FAU-ZTC-800, (c) FAU-ZTC-900, and (d) FAU-ZTC-1000 samples.

Fig. 3. N_2 adsorption/desorption isotherms (A), and pore size distrubution (B) of (a) parent FAU, (b) FAU-ZTC-800, (c) FAU-ZTC-900, and (d) FAU-ZTC-1000 samples.

Fig. 4. (A) Cyclic voltammetry curves, (B) galvanostatic charge-discharge curves, (C) cycle performance, (D) rate performance, and (E) Nyquist plot of FAU-ZTC-900 anode.

Fig. 5. (A) Successive adsorption energies of sodium ions in the ZTC supercages as a function of the filling degree (number of sodium ions added), and relaxed configurations for the adsorption of (B) 2 sodium ions, (C) 24 sodium ions, and (D) 48 sodium ions. The brown and yellow balls represent the carbon and sodium atoms, respectively.

FIGURES

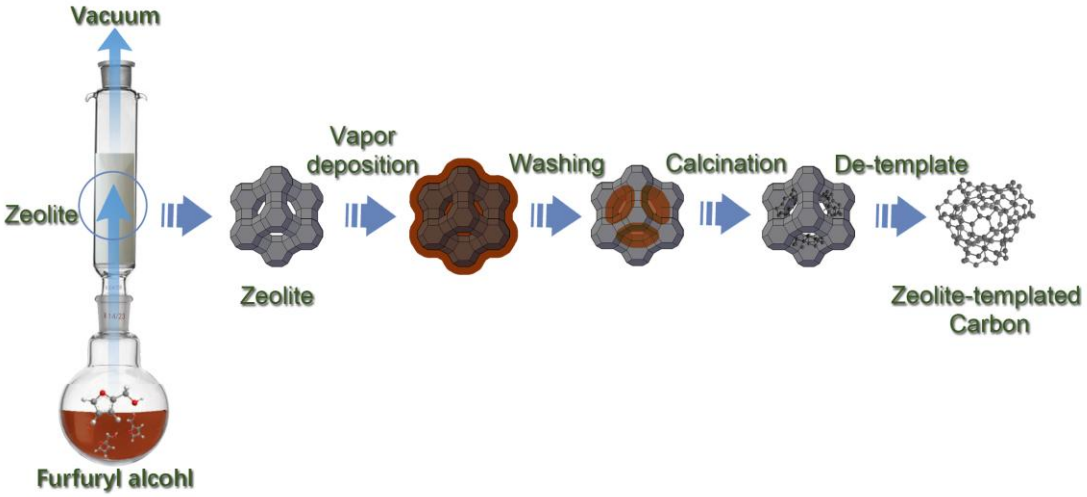

Fig. 1

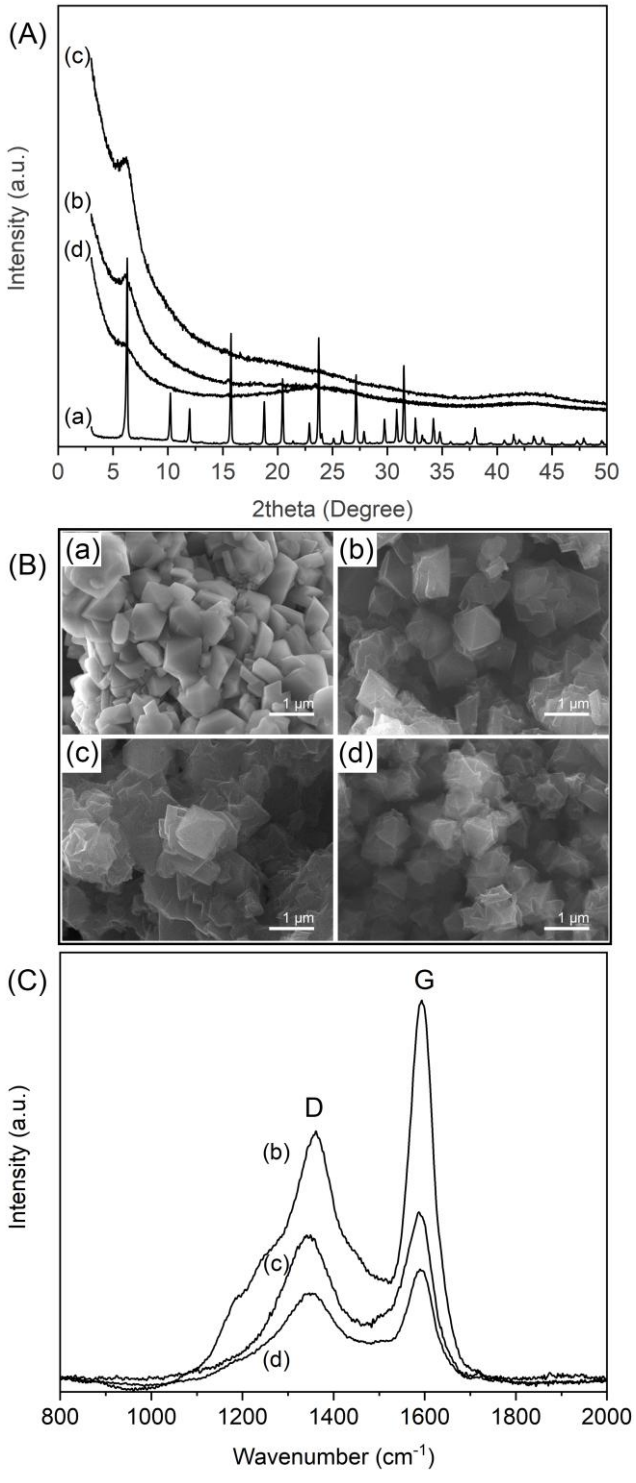
(A)
(c)
(b)
(d)
(a)
Intensity (a.u.)
0 5 10 15 20 25 30 35 40 45 50
2theta (Degree)
(B)
(a)
(b)
(c)
(d)
1 μm
(C)
G
D
(b)
(c)
(d)
Intensity (a.u.)
800 1000 1200 1400 1600 1800 2000
Wavenumber (cm-1)

Fig. 2

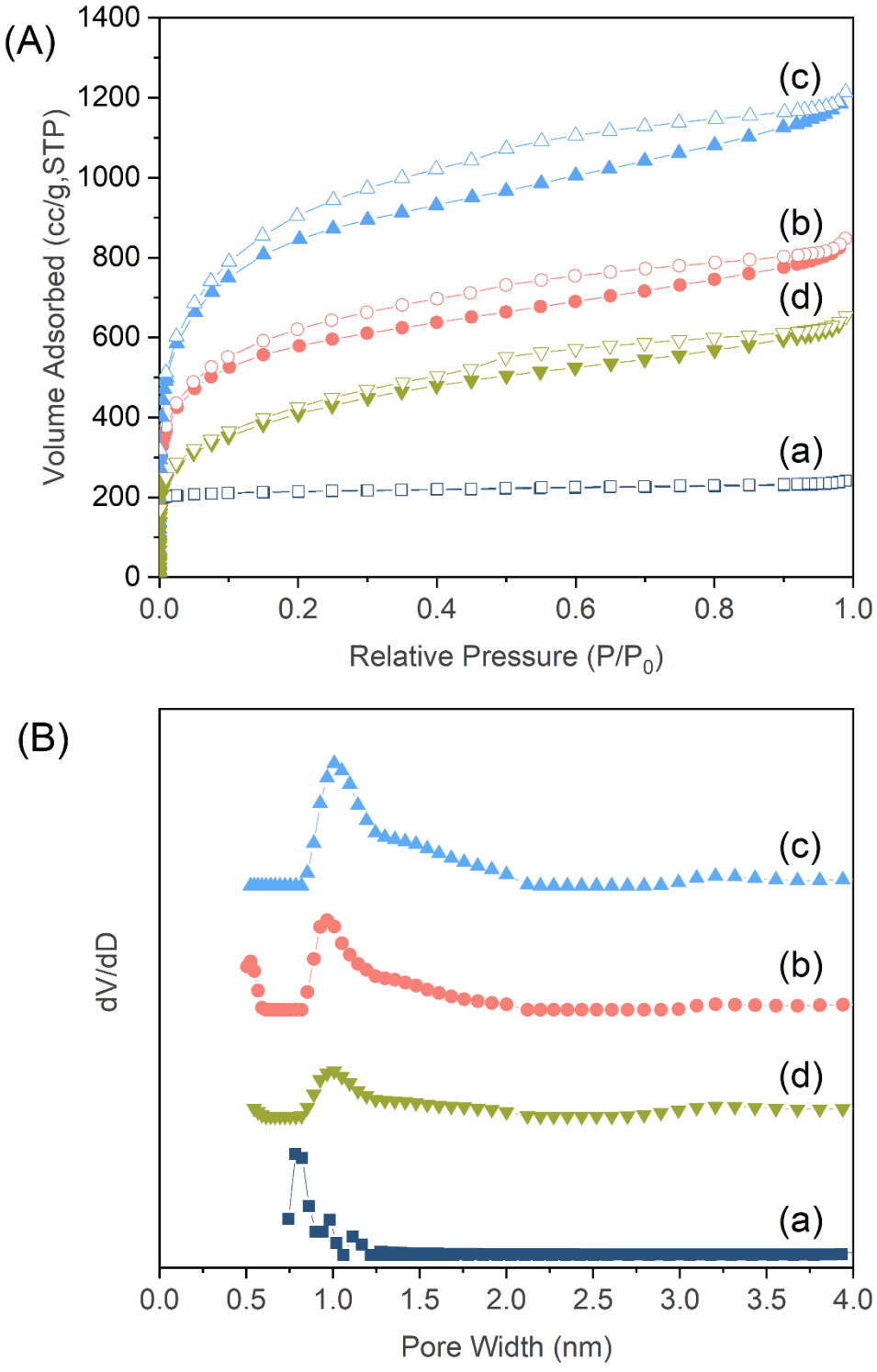
(A)
Volume Adsorbed (cc/g,STP)
Relative Pressure (P/P0)
(a)
(b)
(c)
(d)
(B)
dV/dD
Pore Width (nm)

Fig. 3

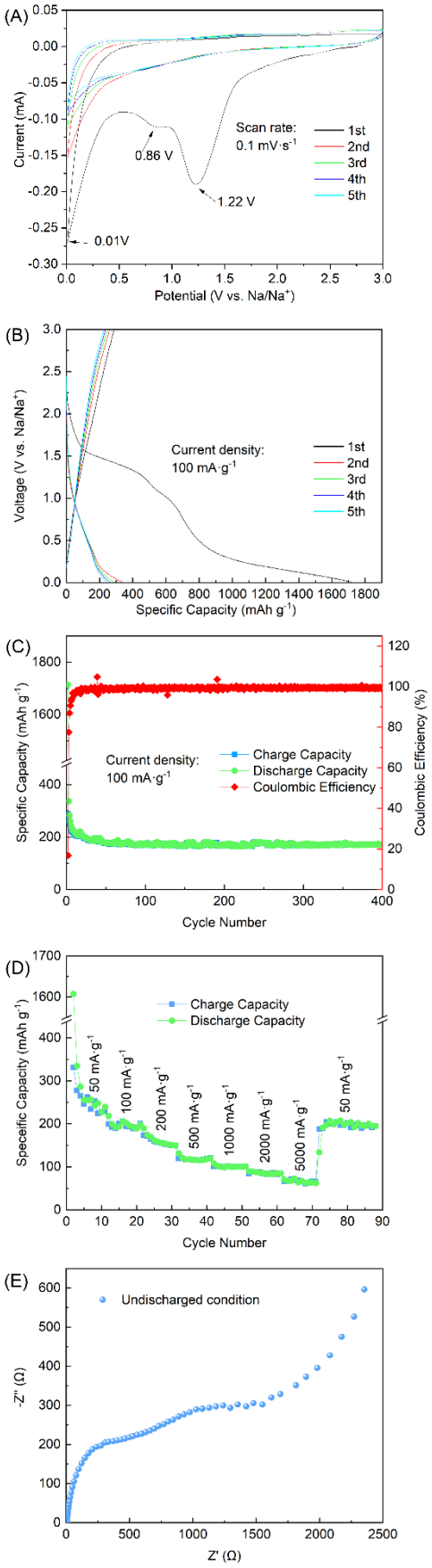
(A)
Current (mA)
Potential (V vs. Na/Na+)
Scan rate:
0.1 mV·s-1
1st
2nd
3rd
4th
5th
0.86 V
1.22 V
0.01V
(B)
Voltage (V vs. Na/Na+)
Specific Capacity (mAh g-1)
Current density:
100 mA·g-1
1st
2nd
3rd
4th
5th
(C)
Specific Capacity (mAh g-1)
Coulombic Efficiency (%)
Cycle Number
Current density:
100 mA·g-1
Charge Capacity
Discharge Capacity
Coulombic Efficiency
(D)
Speceific Capacity (mAh g-1)
Cycle Number
Charge Capacity
Discharge Capacity
50 mA·g-1
100 mA·g-1
200 mA·g-1
500 mA·g-1
1000 mA·g-1
2000 mA·g-1
5000 mA·g-1
50 mA·g-1
(E)
-Z'' (Ω)
Z' (Ω)
Undischarged condition

Fig. 4

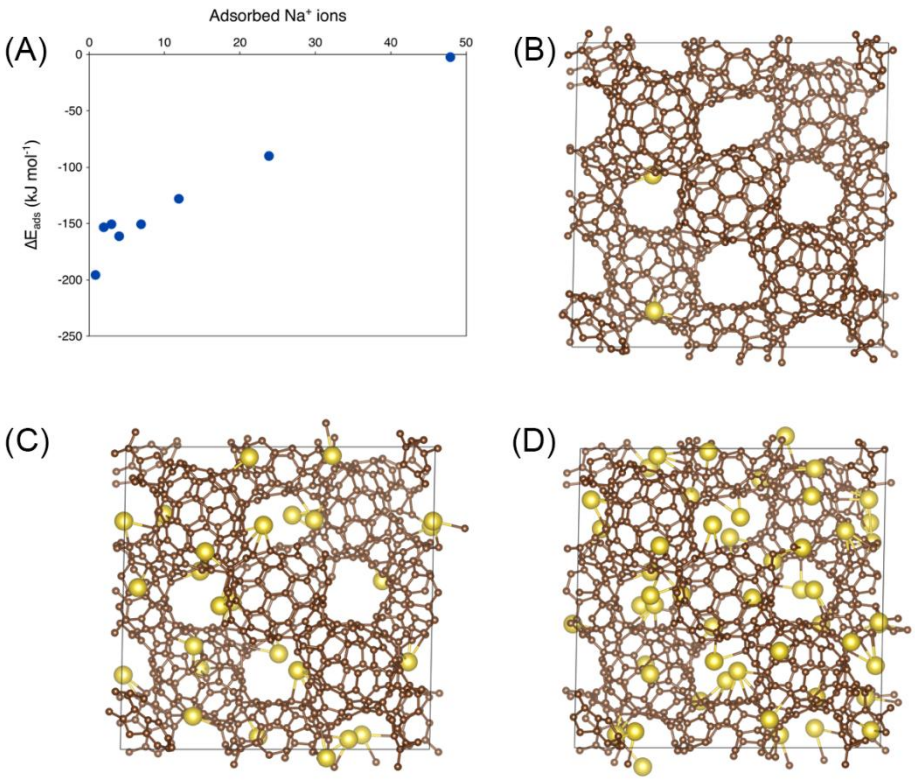
(A)
Adsorbed Na⁺ ions
0
10
20
30
40
50
0
-50
-100
-150
-200
-250
ΔE_ads (kJ mol⁻¹)
(B)
(C)
(D)

Fig. 5